



Improving subduction interface implementation in dynamic numerical models

Dan Sandiford^{1,2} and Louis Moresi¹

¹School of Earth Sciences, University of Melbourne, VIC, 3010, Australia

²Institute of Marine and Antarctic Studies, University of Tasmania, TAS, 7004, Australia

Correspondence: Dan Sandiford (dan.sandiford@utas.edu.au)

Abstract. This study focuses on methodological issues related to dynamic subduction zone modelling. Numerical models often employ an entrained weak layer (WL approach) to facilitate decoupling between the subducting and overriding plates. In such a setup, the kinematics of the flow lead to width variations in the subduction interface. When a uniform-width interface is prescribed, a transient evolution of the interface thickness occurs, during which the volumetric flux along the interface profile establishes equilibrium. Width variations can exceed $4\times$ during this stage, which may impact the effective strength of the interface, both through physical effects if the rheology is linear, and numerical effects if the fault becomes poorly resolved. This transient process induces strong sensitivity to model resolution, and may present a significant challenge to reproducibility. Developing more robust ways to model the subduction interface will enable fully dynamic models to address sensitive subduction-zone processes, such as metamorphism near the slab top. In this study we discuss a simple strategy aimed at improving the standard WL approach. By prescribing a variable thickness weak layer at the outset of the model, and by controlling the limits of the layer thickness during the model evolution, we find improved stability and resolution convergence of the models.

1 Introduction

Subduction zone modelling, both through numerical and analogue experiments, has provided important insights into the dynamic and chemical processes associated with solid earth convection. Yet designing numerical subduction experiments that are simple enough to allow a tractable study of these phenomena, yet rich enough to be quantitatively constrained by the observations remains challenging (Buitter and Ellis, 2016). The subduction interface is a critical and sensitive component in such models. It must simultaneously provide strong strain localisation, low stress, lateral translation, and long term stability (Gurnis and Hager, 1988; Arcay, 2012).

The process of stable asymmetric subduction requires that the down-going plate is substantially decoupled¹ from the overriding plate along the subduction interface (Gerya et al., 2008). In the majority of subduction zones, decoupling transitions rapidly to complete slab-mantle coupling at a depth of around 80 km (Wada and Wang, 2009). This means that the depth extent

¹In this study we use the term coupled in the long-term sense, specifically to the depths where the slab and mantle become continuously coupled ($\gtrsim 80$ km). While seismologists often refer to seismogenic megathrusts as coupled (or locked), from the long term perspective, the plates are decoupled at the megathrust.



of decoupling is significantly greater than the limit of the locked megathrust zone (< 50 km). The subduction interface zone is characterised by rheological and petrological complexity, low strength (relative to the slab), as well as the abundance of water and the critical role of fluid pressure (Bachmann et al., 2009; Bebout and Penniston-Dorland, 2016; Gao and Wang, 2014; Hardebeck, 2015; Duarte et al., 2015; Abers, 2005; Audet et al., 2009).

5 Determining the combination of processes that allow plate-bounding faults to develop is a longstanding problem in geodynamics (Trompert and Hansen, 1998; Moresi and Solomatov, 1998; Tackley, 2000; Lenardic and Kaula, 1994; Bercovici, 2003; Bercovici and Ricard, 2014). Even when the subduction interface is assumed *a priori*, the implementation within a continuum modelling framework is not trivial. Accordingly, a range of modelling approaches have been developed. Different approaches may reflect the style of model (e.g. instantaneous vs. long term), physics and boundary conditions (kinematic vs. dynamic),
10 as well as numerical method (finite difference vs. finite element methods vs. boundary element methods). The most common approach in long term, fully dynamic models is to implement the subduction interface as a continuously-entrained layer of weak material (WL). While the WL approach has been utilised in a broad range of studies, a detailed analysis of the technical implementation is lacking (although valuable insights appear in Arcay (2017); Manea and Gurnis (2007); Arcay (2012); Čížková et al. (2002); Androvičová et al. (2013)). In this paper we focus on the dynamics and evolution of the subduction inter-
15 face material under the WL approach. The results have relevance for model reproducibility and provide a basis for improving precision within fully dynamic models.

2 The subduction interface

The subduction interface refers to the plate boundary fault at earth's convergent margins. Exhumed subduction interfaces are typified by melange zones, often 100's of meters in width, with coherent blocks embedded within a sedimentary and/or
20 serpentinitised matrix (Kimura et al., 2012; Bebout and Penniston-Dorland, 2016; Lallemand, 1995; Vannucchi et al., 2008; Shreve and Cloos, 1986; Vannucchi et al., 2008). Entrainment of sediment at subduction is highly variable (Shreve and Cloos, 1986; Huene and Scholl, 1991). Subducted sediments can reach depths of up to 80 km (Bayet et al., 2018), similar to the inferred depth at which the slab and mantle become coupled, and can be traced in the composition of arc magmas (Plank and Langmuir, 1993). The proportion of subducted sediment may lead to large variations in the mechanical properties in the deep
25 subduction interface Behr and Becker (2018). Whether these variations have an observable impact on subduction dynamics is debated, partly due to the complex set of controls on plate velocities (Duarte et al., 2015; Schellart and Rawlinson, 2013; Cloos and Shreve, 1988; Behr and Becker, 2018). Entrainment of upper plate material in a process known as subduction erosion also occurs at a substantial number of convergent margins (Huene and Scholl, 1991). Subduction interfaces therefore incorporate material from the subducting plate, the accretionary prism, and the upper plate (Vannucchi et al., 2008). The deeper part of
30 subduction interface where the slab is in contact with the serpentinitised upper-plate mantle is thought to be controlled primarily by weak hydrous minerals which allow effective slab-mantle decoupling but also inhibits unstable seismic slip (Hirauchi and Katayama, 2013; Reynard, 2013). The thickness of subduction interfaces, particular in the deeper aseismic zone, is not well constrained. Estimates range from between 10's metres to a few kilometres (Vannucchi et al., 2012, 2008; Abers, 2005; Cloos



and Shreve, 1988). Behr and Becker (2018) used structural relationships in exhumed subduction interfaces to infer the relative strength of different lithologies. Metasediments and serpentinites which commonly form the matrix within the subduction melange appear to be weakest.

In the shallow megathrust, pore fluid water and clay minerals are thought to exert a major control on the rheology (Vrolijk, 1990). At greater depths, fluids are generated by devolatilization reactions (Bebout and Penniston-Dorland, 2016). Seismic imaging demonstrates the presence of fluids along the plate boundary (Audet et al., 2009). In some cases pore pressures are inferred to be near lithostatic values (Audet et al., 2009). Fluid pressure plays a key role in subduction zones interfaces as it determines the effective frictional strength, controls the seismic/aseismic character of slip (Audet and Schwartz, 2013) and dictates the extent of hydrous mineral formation along the subduction interface (Reynard, 2013).

While many subduction zone megathrusts are capable of hosting great earthquakes, there is a spectrum of behaviour from locked to creeping. Ongoing debate surrounds the strength implications of this divergent behavior (Gao and Wang, 2014; Hardebeck, 2015; Hardebeck and Loveless, 2018). The limit of the seismogenic zone can range from 5 to 50 kilometres in depth, and is usually found to reside in the forearc mantle, rather than crust (Wang, 2010; Wada and Wang, 2009). The topography of most forearcs is consistent with average shear stresses of 15 MPa over the long-term (Lamb, 2006). Heat flow studies, combined with full thermal modelling of particular subduction zones are generally consistent with megathrust shear stresses in the range 1-100 MPa with mean shear stresses around 15 MPa (Peacock, 1996; Gao and Wang, 2014). It remains unclear whether the rheology of the deep subduction interface is dominated by viscous or (stable) plastic behavior (Li and Ghosh, 2017; Proctor and Hirth, 2016).

Phyllosilicates such as serpentine, chlorite and talc are inferred to have a strong influence on subduction zone dynamics because of their high water content and low strength at shallow and intermediate depths (Hilaret and Reynard, 2009; Schmidt and Poli, 1998; Hirauchi and Katayama, 2013). Serpentine minerals form by hydration of olivine at the boundary of the slab and mantle wedge, where fluids from the subducting slab accumulate. Their stability range extends to 550°C and 200 km depth (Reynard, 2013). Chlorite forms primarily through hydration of orthopyroxene, another abundant mineral in dry peridotite. Talc typically forms by metasomatic alteration of the wedge through addition of silica-rich hydrous fluids derived from the slab. At the subduction interface the most stable serpentine polymorph, antigorite, is limited to depths between 70 to 120 km, depending on the thermal regime. This serpentinised (plus chlorite, talc) layer at the top of the slab is thought to be primarily responsible for accommodating decoupling to ~ 80 km (Hilaret and Reynard, 2009; Ulmer et al., 1995).

3 Past modelling approaches

In efforts to study subduction zone dynamics, a range of modelling approaches have been developed. The subduction interface is a necessary model component whenever both subducting and upper plates are included. One approach is to incorporate the interface directly as a kinematic constraint into the simulation, i.e. by specifying continuous normal and discontinuous tangential velocities in the model solution surrounding the fault (Billen et al., 2003; Christensen, 1996). This idea was developed into a fully dynamic framework with finite element models that incorporate internal stress boundaries; the result is zero

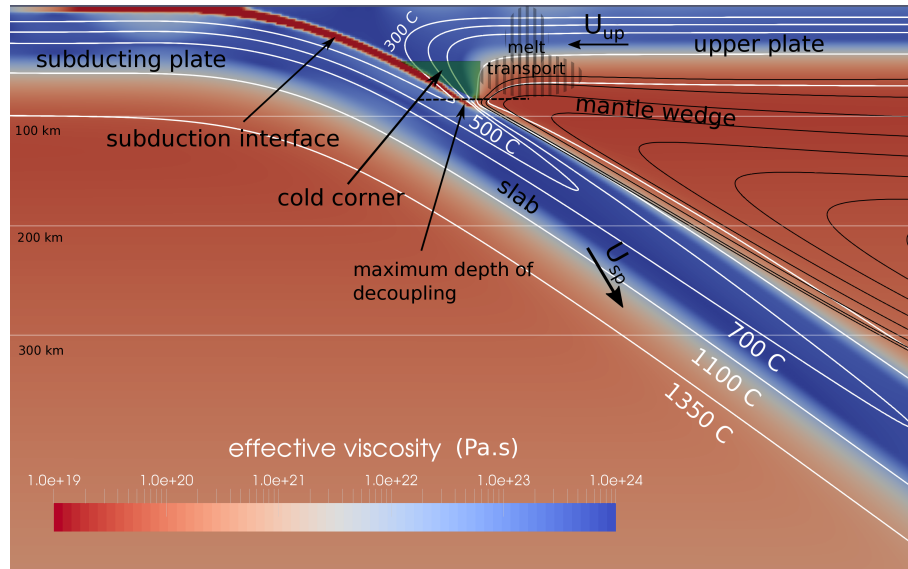


Figure 1. Example of numerical dynamic subduction simulation. Closeup of the slab in the upper mantle from a fully dynamic subduction model. Colormap shows the effective viscosity, and reveals the weak finite-width subduction interface which enables decoupling of the slab and the upper-plate. In this model the subduction interface has a simple constant linear viscosity. The implementation of the interface follows the embedded fault (EF) strategy developed in this study. The subduction interface extends to 100 km depth, beyond which the slab and mantle become coupled. Dynamically, this is known as the Maximum Depth of Decoupling (MDD). Above the MDD part of the mantle wedge tends to become stagnant due to the strong temperature dependence of the rheology. This is often referred to as a ‘cold corner’, depicted here with a green polygon. The region labelled *melt transport* is representative.

width faults within the continuum mechanical representation of the lithosphere (Zhong and Gurnis, 1992, 1995; Aagaard et al., 2008). Because moving mesh nodes are needed to capture proper fault advection, accurate tracking of large scale deformation is challenging. A more common approach is to apply finite regions of weak constitutive behavior within a static mesh. The velocity field naturally develops strain localization around the weak zone, although the ‘faults’ are usually very much broader than real plate boundaries. This approach was first applied as a spatially-fixed low viscosity zone that could decouple the plates but would not allow trench motion (e.g. Gurnis and Hager, 1988). This type of implementation was developed so that narrow low-strength weak zone ‘stencils’ could also be advected to allow trench motion (Kincaid and Sacks, 1997; Billen and Hirth, 2007).

Over the past decade the use of an entrained weak layer (WL) has become an increasingly common strategy (e.g. Capitanio et al., 2010; Garel et al., 2014; Holt et al., 2015; Agrusta et al., 2017; Magni et al., 2012; Babeyko and Sobolev, 2008; Čížková and Bina, 2013; Glerum et al., 2017; Arredondo and Billen, 2017; Chertova et al., 2012). Rather than using a fixed weak zone, the subduction interface is typically implemented by imposing a material layer at the top of the subducting plate that is advected with the flow and continuously entrained into the decoupling region. The WL approach enables a mobile trench while also helping to facilitate plate bending as it enters the subduction zone (even in the absence of free surface). Additionally, it



isolates the extremely weak parts of the system (the plate boundary) from the plates, enabling long-term asymmetric subduction to occur. The WL implementation will often include decisions about where to create and remove the weak material after it has passed through the zone of decoupling. Similarly, choices are often made about where the weak material will be created, for instance across the entire upper boundary of the model, just the subducting plate, or part of the subducting plate only. In this study, we do not attempt to examine all the permutations of the WL approach that appear in previous model. Rather, we focus on the most basic and common aspects the WL implementation. The analysis considers both the physical evolution of the layer, as well the implications from a numerical and modelling standpoint.

There is degree of ambiguity as to whether the WL approach represents an attempt to explicitly model subduction interface dynamics, or should instead be conceived as an solution to the sub-grid scale physics of faulting. This also reflects complexity in the physical system, as the shallow subduction interface is probably more fault like, while the deeper interface may be more channel-like Gerya et al. (2002); Behr and Becker (2018). WL implementations do mimic several critical processes that are thought to contribute to the weakness of the subduction interface. One of these is the process of entrainment or ‘self-lubrication’ (Lenardic and Kaula, 1994). The entrainment of a range of materials along the slab interface likely plays a key role in maintaining subduction interface weakness. Additionally, the WL approach might be linked with deformation-localizing processes such as damage, grain size reduction, fabric development. Indeed, WL models have been conceived as a limiting case in which comprehensive damage is assumed within the interface material and hence can be prescribed at the outset (Tagawa et al., 2007). Whichever way the WL is conceptualized, the primary requirement is to establish a sufficient decoupling between the plates. If the imposed interface is too strong, subduction will be unrealistically slow, or may entrain the upper plate in a mode of catastrophic buckling and failure.

The behavior of subduction interface in numerical models is discussed in some detail in Arcay (2012, 2017). These studies highlight the tendency for the subduction interface to develop spontaneous thickness variation as the models progress. Typically the interface widens near the trench, building a prism-like complex, and thins at depths beyond the brittle-ductile transition at around 50 kms depth. This pattern was also noted in the boundary element models of (Gerardi and Ribe, 2018), who attributed it to lubrication layer dynamics. Because of this tendency, Arcay (2017) proposes that to achieve proper resolution, one must preemptively over-resolve the interface. A related issue is that many dynamic WL formulations are likely to evolve towards maximum subduction interface thickness around twice the imposed thickness, a phenomena we explore in this study. For instance, a model with a prescribed weak layer of 5 km is likely to develop an maximum thickness throughout the decoupling region of 10 km. Understanding and controlling these unintended width variations will be vital in terms of using dynamic models to explore sensitive subduction-zone processes, such as metamorphism and melting near the slab top. Currently, these type of questions are mainly addressed using thermo-kinematic models. Bench-marking of community codes indicates that precision to about 1 km, & 20°K can be expected in well resolved thermo-kinematic models (van Keken et al., 2008). This provides a useful, if ambitious target for dynamic numerical subduction models.



4 Methods

4.1 Numerical model setup

The numerical subduction models developed in this study represent the time evolution of simplified conservation equations for mass, momentum and energy within a 2D Cartesian domain. Solutions to the equations are derived using a Galerkin finite-element approximation. Fig. 2 provides an overview of the model domain, as well as initial and boundary conditions. The depth of the domain is 1000 km, and the aspect ratio is 5. Initial temperature conditions define two plates which meet at the centre of the domain, including a small asymmetric slab following a circular arc. The subducting plate has a initial age of 50 Myr at the trench, while the upper plate age is 10 Myr. Both plates have a linear age profile with initial age of zero at the sidewalls. The initial conditions allow for self-sustaining (fully-dynamic) subduction to proceed. There is no compositional difference between the subducting (oceanic) and upper (continental) plate nor any compositional differentiation within the oceanic lithosphere. The only aspects of the model setup that are varied are the details of subduction interface implementation (described in the following section) and the model resolution. The mantle is treated as an incompressible, highly viscous fluid in which inertial forces and elastic stresses can be neglected. The mechanical behaviour of mantle (including the thermal lithosphere) is prescribed by a composite rheological model that includes a linear high-temperature creep law, as well as a scalar visco-plastic flow law, sufficient for capturing psuedo-brittle as well as distributed plastic deformation within the slab. Thermal buoyancy is the only source of density variation in the model. The thermal variations are coupled to the momentum equation through their effect on density, which follows the Boussinesq approximation. A detailed description of the governing equations, constitutive laws, and physical parameters are given in Appendix A.

Approximate solutions to the incompressible momentum and energy conservation equations are derived using the finite element code *Underworld 2*. Underworld2 is a Python API (Application Programming Interface) which provides functionality for the modelling of geodynamic processes. Underworld2 solves the discrete Stokes system through the standard mixed Galerkin finite element formulation. The domain is partitioned into quadrilateral elements, with linear elements for velocity and constant elements for pressure (Q_1/dP_0) (Arnold and Logg, 2014). The typical models discussed in this chapter have a mesh resolution of 160 elements in the vertical direction, refined to provide a element width of ~ 2 km at the surface. Material properties are advected on Lagrangian tracer particles, with 30 tracers per element. During quadrature, material properties are mapped to quadrature points using nearest-neighbour interpolation. The Lagrangian tracer particles are used to distinguish the subduction interface material from the rest of the system (lithosphere and mantle). Underworld2 solves the energy conservation equation using an explicit Streamline Upwind Petrov Galerkin (SUPG) method (Brooks and Hughes, 1982). In this approach, a Petrov-Galerkin formulation is obtained by using a modified weighting function which affects upwinding-type behaviour. The Stokes system has free-slip conditions on all side and bottom boundaries. The energy equation has constant (Dirichlet) and zero-flux (Neumann), on the top and bottom boundary respectively. The right hand sidewall has a constant (potential) temperature which enforces a ridge at that boundary. The left and right sidewalls have a constant potential temperature of the mantle is 1673°K , and the surface temperature is 273°K .

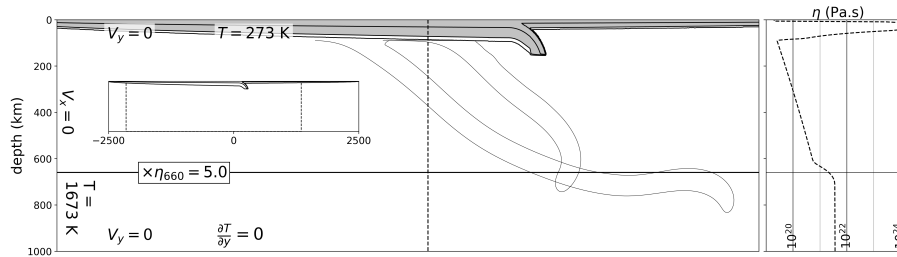


Figure 2. Initial conditions for 2D thermo-mechanical subduction models. All models in this study models have a 50 Myr initial slab age, and free-slip boundary on upper boundary. The dark gray region in main panel shows parts of the model colder than $1100\text{ }^{\circ}\text{C}$. Inset shows the full domain. Outlines of the slab is shown at later times: 10 & 20 Myr. Right hand panel shows viscosity profile along the vertical dashed line in main panel.

4.2 Subduction interface implementation

The focus of our study is a common approach to modelling the subduction interface, referred to here as continuously entrained weak layer (WL). Past studies have also termed this a weak crust. Generally, this approach have two defining attributes: 1) the material that provides decoupling within interplate zone is a distinct material type contrasting with the background material (Billen and Hirth, 2007; Garel et al., 2014; Čížková and Bina, 2013; Arredondo and Billen, 2017; Agrusta et al., 2017) and 2) the weak material layer is distributed along some or all of the subducting plate, so that the flow itself entrains new weak material into the decoupling region. Throughout this study, we refer to a standard WL approach as one in which the distribution of weak is fully self-evolving within the deforming subduction interface zone. We also demonstrate an improved version of this approach, which we refer to as an embedded fault (EF). The EF implementation includes a reference line advected along the base of the weak layer. The reference line provides a way to constrain the minimum and maximum thickness of the weak layer material, (i.e. to alter the material distribution within the model by setting subduction interface particles to background particles² and vice versa). The relationship between the EF tracer line, the global swarm, and the mesh is shown in Fig. 3. In the EF approach, we also initialise the weak material with a non-uniform thickness. Within the interplate zone, the weak material will typically have twice the thickness that is prescribed on the top of the subducting plate. The choice emerges from the behavior we observe in the standard WL models, as discussed in the following section.

It is important to emphasise that differences between the WL and EF implementations relate only to the distribution of weak material within the model. All other aspects of the interface representation remain identical. Weak material is continually prescribed along the upper-most part of the subduction plate, with a specified constant thickness ($W_{\text{init}} = 10\text{ km}$). Meanwhile, the upper plate does not contain any weak/interface material. For simplicity, there is no rheological variation between the shallow (frictional) megathrust and the deeper, viscous interface. A depth-dependent cosine taper is used to transition the subduction interface rheology to the background mantle rheology. The transition is imposed by a static depth dependent function. In this

²In this study Lagrangian tracer particles are used to track material properties. Mesh/field based methods have also been used to implement a WL (e.g. Garel et al., 2014).

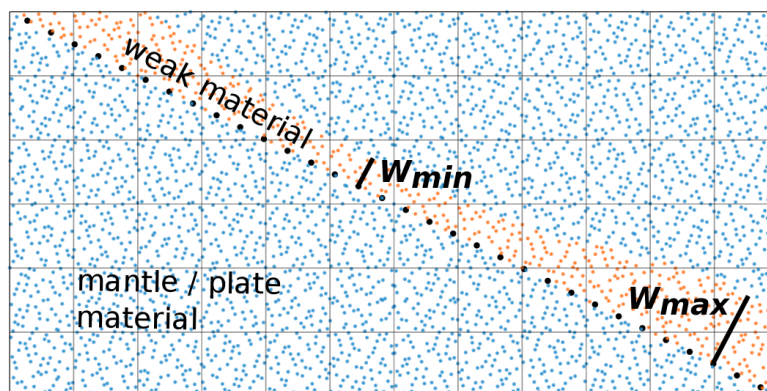


Figure 3. Schematic of the embedded fault (EF) implementation. The EF is a modification to the standard weak layer (WL) approach. As with the WL, shear localization along the subduction interface is encouraged by a finite-width layer of weak material (orange particles). In the EF approach, a line of tracer particles (black points) is advected with the flow, at the base of the interface. This line provides a set of reference points to enforce width limits on the weak material, denoted by W_{\min} and W_{\max} . This approach mitigates the strong thinning of the layer that occurs in the standard WL approach (see Fig. 4), and also reduces short-wavelength instabilities that develop at the boundary between the subduction interface and the upper plate.

chapter the cosine taper for the transition (both WL and EF) begins at 100 km, and has a width of 30 km. This type of behavior is very simple to implement using the Underworld2 function capability. Decoupling is strongly inhibited at depths greater than the taper onset. Hence the depth of the taper onset (100 km) effectively sets the maximum depth of decoupling, as shown in Fig. 8.

5 Results

5.1 Analysis of weak layer approach

In a number of previous studies it was observed that the WL approach tends to develop spontaneous variations in the interface thickness (Arcay, 2017; Duretz et al., 2012; Gerardi and Ribe, 2018). Here we identify two separate causes for these thickness variations. The first can be understood as an outcome of the evolution towards uniform volumetric flux along the interface. This phenomenon is likely to be present in any implementation of the WL approach. The second represents shorter-wavelength instabilities at the boundary between the subduction interface and the upper plate. Both of these characteristic behaviours can be seen in Fig. 4, where we plot the interface thickness as a function of the downdip distance during 20 million years of model evolution. During the first few million years of the model evolution, changes in the interface thickness have both spatial and

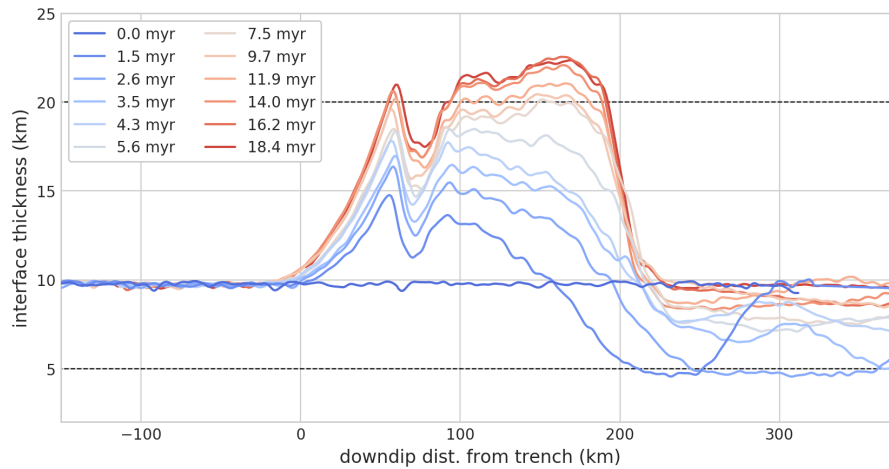


Figure 4. Interface thickness evolution in WL implementation. The initial layer thickness (W_{init}) is 10 km. Colored lines show the evolving thickness plotted as function of downdip distance from the trench.

temporal dependency. The interface thickens at distances of up to 150 km downdip from the trench, whereas beyond this it thins. The point of zero thickness change (10 km) migrates downdip with time. The interface reaches a minimum thickness of around 5 km at ~ 2.0 Myr, while it reaches 20 km, close to its maximum thickness, at around 7 Myr. The thickened part of the interface evolves to a near-constant configuration, both in thickness (~ 20 km) and downdip extent (~ 200 km). In contrast the thinning of the deeper interface is transient and by ~ 15 Myr the deeper part of the interface has reestablished a thickness close to the initial value (10 km). In the following section we provide a simple explanation for these systematic width variations, based on a simplified kinematic description of flow within the WL.

In the WL approach, interface thickness variations appear to be a simple outcome of the evolution towards uniform volumetric flux along the interface. The flux is a function of both the interface thickness as well as the effective boundary conditions on the interface. In the following discussion we refer a slab-based coordinate system, where \hat{y} is the direction orthogonal to the slab midplane, and \hat{s} is a vector parallel to the slab midplane. Before reaching the trench, the weak interface material travels with the subducting plate, with effectively uniform velocity and zero shear ($\frac{\partial V_s}{\partial \hat{y}} = 0, V_s = V^{conv.}$). In the interplate region, however, the weak interface material decouples the slab and upper plate, and the velocity gradient is finite. For a Newtonian rheology, the gradient is expected to be linear with $\frac{\partial V_s}{\partial \hat{y}} = \frac{V^{conv.}}{W}$ (i.e. Couette flow). This change in velocity gradient means that the volumetric flux across the interface is reduced, compared to the flux of interface material arriving on the incoming subducting plate. This causes material to accumulate at the trench, progressively thickening the interface from the top down. Assuming a linear velocity profile, the volume flux will reach equilibrium when the thickness of the decoupling region is twice the prescribed thickness (i.e. the thickness on the top of the subducting plate). This is consistent with the equilibrium thickness of the interface that develops in the WL models (e.g. Fig. 4). At the base of the subduction interface the slab and mantle flow becomes coupled (sometimes referred to as the Maximum Depth of Decoupling - or MDD). When a constant interface width



is prescribed, the interface thickness at the MDD initially decreases because the volumetric flux increases at the MDD, as the decoupling region (Couette flow) transitions to the fully coupled flow. In effect, we see a reversal of the process that occurs at the top of the subduction interface. The location where the subduction interface thins is a proxy for the MDD, again because of the relationship between the flow kinematics and volumetric flux. In typical thermo-mechanical subduction model setups, the MDD is unlikely to be constant. Instead the MDD tends to become deeper as the corner of the mantle wedge cools and stagnates (see Fig. 8).

A simple boundary-driven Stokes flow provides a useful analogy to the thickness evolution of the subduction interface in the WL approach. This boundary-driven model consists of an incompressible Newtonian fluid that transitions from uniform flow to Couette flow, due to a change in the mechanical boundary condition along one side of the model, from frictionless (or free slip) to frictional (no slip). The material distribution consists of a weaker and a stronger layer as shown in Fig. 5. The step change in boundary conditions imposes horizontal velocity gradients which must be balanced by vertical velocity gradients. The vertical velocity causes the weak layer to thicken near the start of the no slip region, and thin near the end. The width changes of the weak layer proceed until the overall volume flux reaches equilibrium.

Based on analysis of typical WL setup, we see that the primary control on the interface thickness variation is the condition of uniform volumetric flux along the interface. The duration of the transient thickness evolution is driven both by the timescale of accumulation of material as well as by changing kinematics of flow due to deepening of the MDD. In addition to these flux-controlled changes, Fig. 4 shows that the subduction interface also develops a persistent short-wavelength width perturbation just beneath the tip of the forearc at a downdip distance of $\sim 60 - 80$ km. Here the interface thins by $\sim 3 - 4$ km. This occurs in combination with strong, localised plastic deformation in the upper plate. It seems likely that these short-wavelength anomalies may be effected by a range of factors, including the interface and lithosphere rheology, mesh resolution, and material advection scheme. If so, these feature are likely to be rather model/code dependent, in contrast to the to longer-wavelength, flux-related thickness variations.

5.2 Improving the weak layer approach

The embedded fault (EF) implementation, described in Section 4, primarily enables us to control the subduction interface thickness (i.e. the weak layer thickness). In general, this may consist of controlling the minimum thickness (W_{min}), the maximum thickness (W_{max}), or both. Perhaps an obvious first issue to address is what happens if we simply enforce a constant width interface at all times. While this would in some ways be a desirable approach, doing so results in the development of a very spurious subduction morphology. Fig. 7a shows results from such a case ($W_{max} = W_{min} = W_{init}$). After 15 million years of model evolution a very atypical subduction morphology has developed, with an extremely low angle megathrust beneath a forearc region with a width of greater than 600 km. While physically inconsistent, this constant width EF example provides a useful insight into the way in which the interface deformation can influence model dynamics. When the subduction interface is forced to remain at constant width, the interface is unable to evolve towards flux equilibrium. Persistent interface-normal velocity components result, and the compounding effect eventually distorts the morphology of the entire subduction hinge region. Fig. 7b shows the slab morphology developed by instead using $W_{max} = 19 \text{ km} = 1.9 \times W_{init}$ (we discuss the choice of

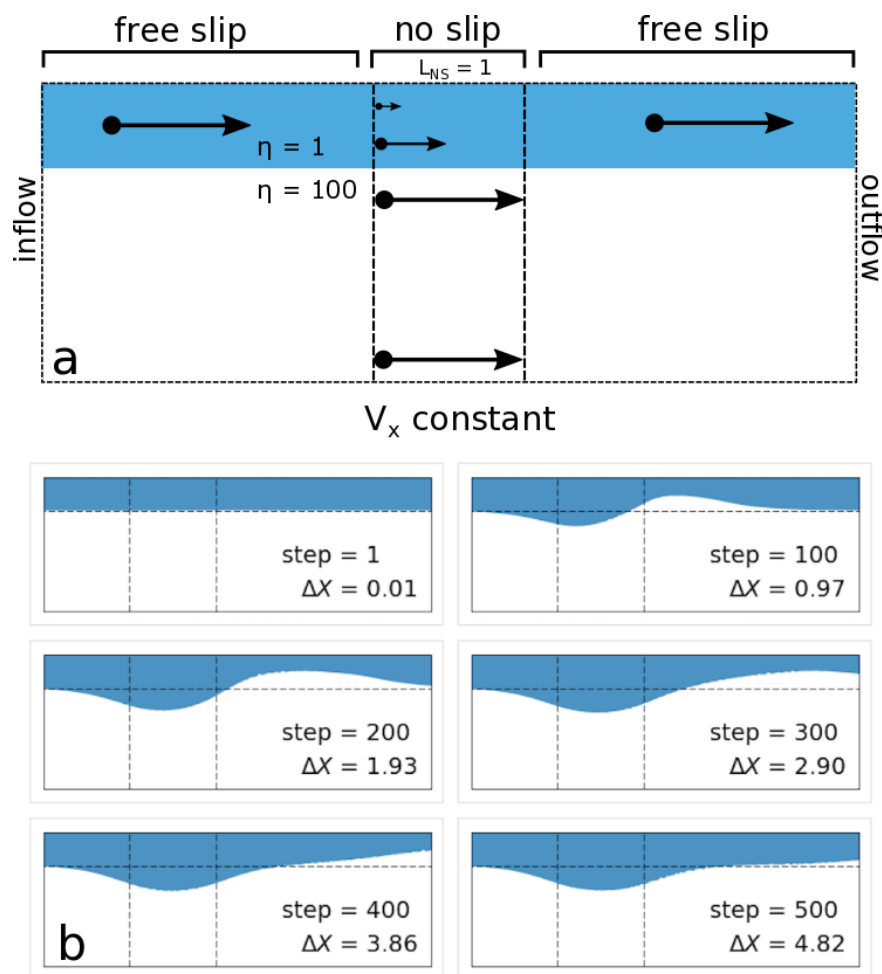


Figure 5. Simple analogue for WL dynamics. a) model setup for a boundary-driven flow where a weak layer (shown in blue) interacts with a stronger layer (white). The top surface of the model is free slip, except for a patch of no-slip nodes ($V_x = 0$). The bottom surface has a constant horizontal velocity component. b) evolution of material in the boundary-driven model. ΔX represents the accumulated displacement along the bottom boundary, normalised by the width of the no-slip patch.

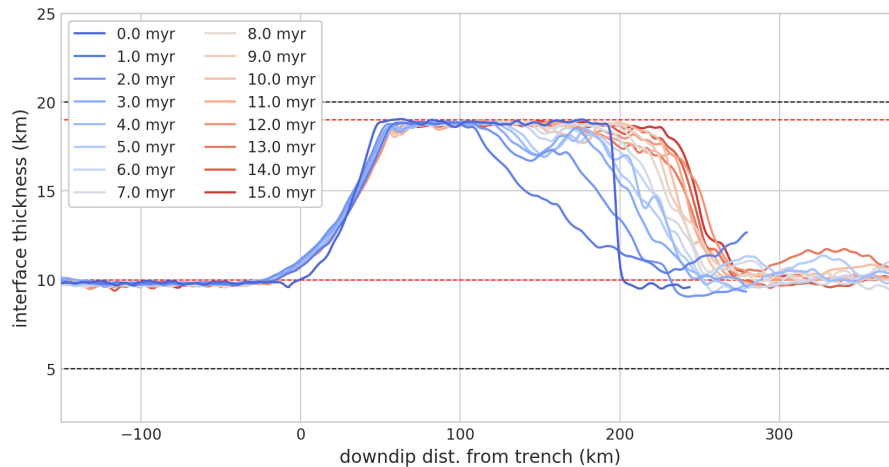


Figure 6. Interface thickness evolution, EF approach. In the EF implementation limits are imposed in the maximum and minimum thickness. Unlike the standard WL approach, the initial thickness of the interface is variable. The initial thickness of the interface within the decoupling region is equal to W_{max} .

1.9 in the next section). The subduction morphology in this simulation is much more realistic, and consistent with the behavior we would expect using standard WL approach. The evolution of the interface thickness from the same simulation is shown in Fig. 6. In addition to controlling the width of the interface throughout the simulation, we have also prescribed the initial interface thickness in the decoupling zone (from the trench to a depth of 100 km depth) to have value equal to W_{max} (19 km). In this way, we have tried to preemptively impose a thickness profile closer to the flux equilibrium. Fig. 6 shows that this strategy reduces, but does not fully eliminate, the transient stage of interface adjustment. It is challenging to fully eliminate the transient stage because the equilibrium interface thickness profile depends critically on the depth of slab mantle coupling (MDD). In this thermo-mechanical subduction setup, the evolution of the MDD is a response to the cooling of the mantle wedge and the development of a stagnant ‘cold corner’ (see Fig. 8). Prescribing initial temperature conditions that include the cold corner, would be one way to further reduce the amount the transient adjustment of the interface.

In addition to the thickness variations related to volumetric flux, there also tends to be short wavelength thickness variations. In the EF implementation, we found that using a W_{max} slightly less than $2.0 \times W_{init}$ helps to suppress short wavelength thickness variations, without significantly effecting the overall model evolution relative to a larger value. In other words, while we need to allow the interface to develop some amount of thickness variation, it may be advantageous to use a value slightly less than $2 \times W_{init}$. Fig. 10 shows the material and interface thickness distribution using WL and EF implementation. Horizontal red lines show the location of W_{max} and W_{min} . One advantage of the EF approach is that it offers improved precision in determining the thickness of the subduction interface. Such precision will be important for studying highly pressure- and temperature-sensitive processes, such as metamorphism and melting near the slab top.

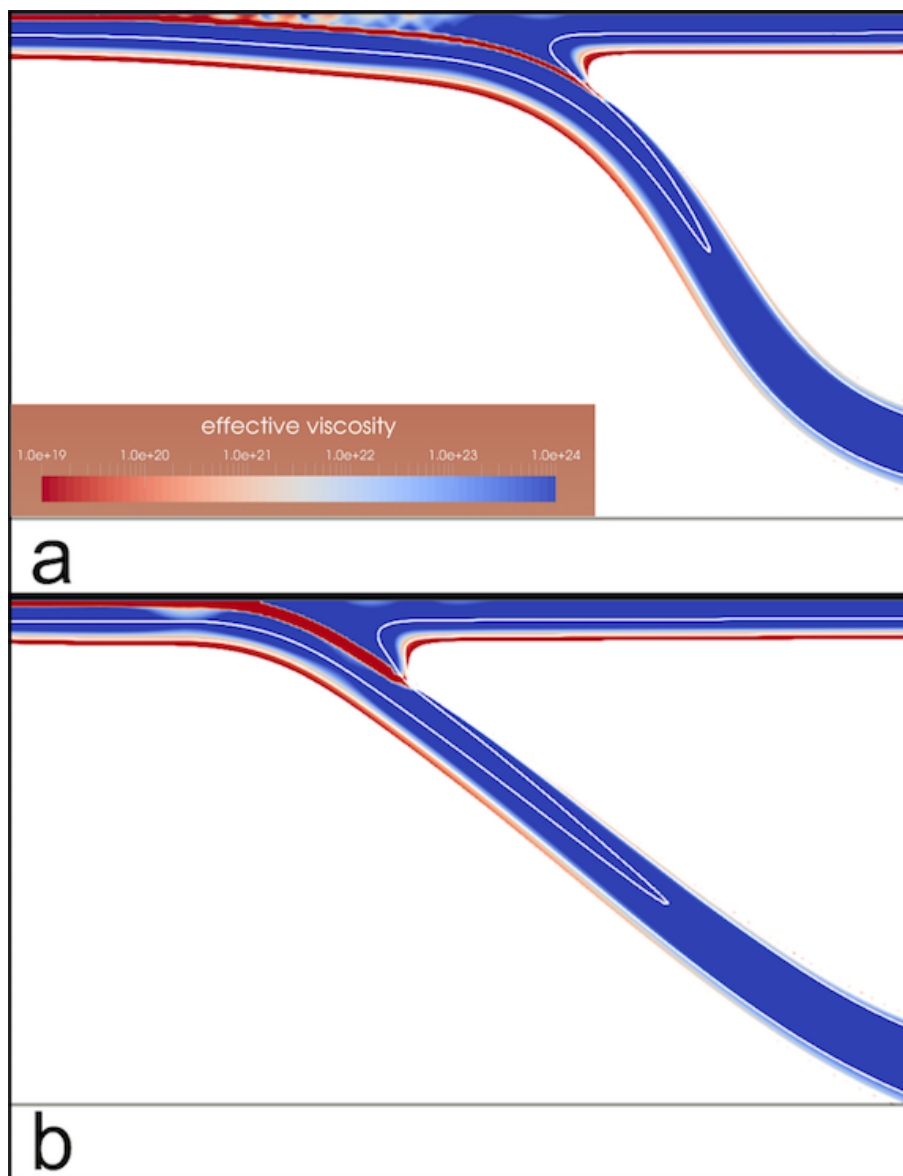


Figure 7. Embedded fault models (EF) with variable W_{\max} . The colormap shows the effective viscosity at a model time of 14 Myr. Parts of the model with temperature above 1250 °C are masked (white). White lines show isotherms at 700 and 1100 °C. a) $W_{\max} = W_{\text{init}} = 10$ km. Note the extremely long, low-angle morphology of the subduction interface that develops when the interface cannot adjust its thickness. b) $W_{\max} = 1.9 \times W_{\text{init}}$. This choice results in a more physically-consistent subduction morphology.

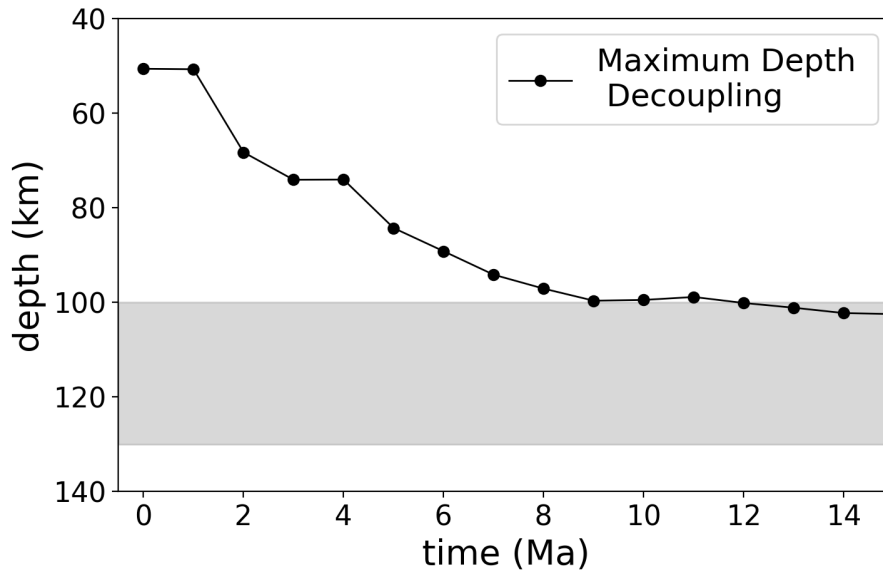


Figure 8. Evolution of the maximum depth of decoupling (MDD). As the mantle wedge cools, it progressively stagnates, requiring deeper decoupling within the subduction interface. The grey region in the figure shows the depth interval over which the subduction interface transitions to the background mantle rheology as prescribed with a cosine taper (see main text and Appendix A for further information on the interface rheology).

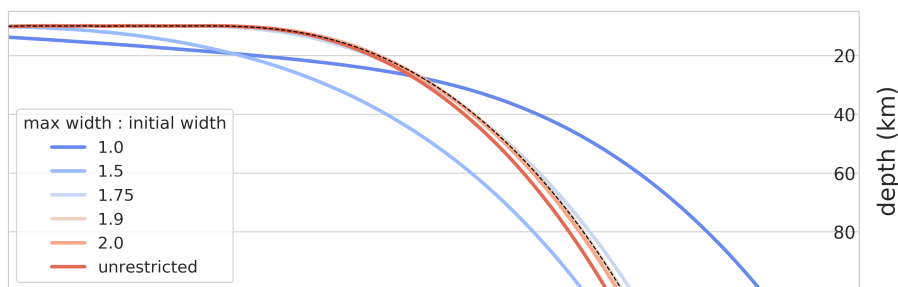


Figure 9. Embedded fault models (EF) with variable W_{\max} . Lines represent the morphology of the base of the subduction interface at 10 Myr for different models with varying W_{\max} . If interface thickness variation is strongly constrained, the evolution of the model is significantly effected. See also Fig. 7.

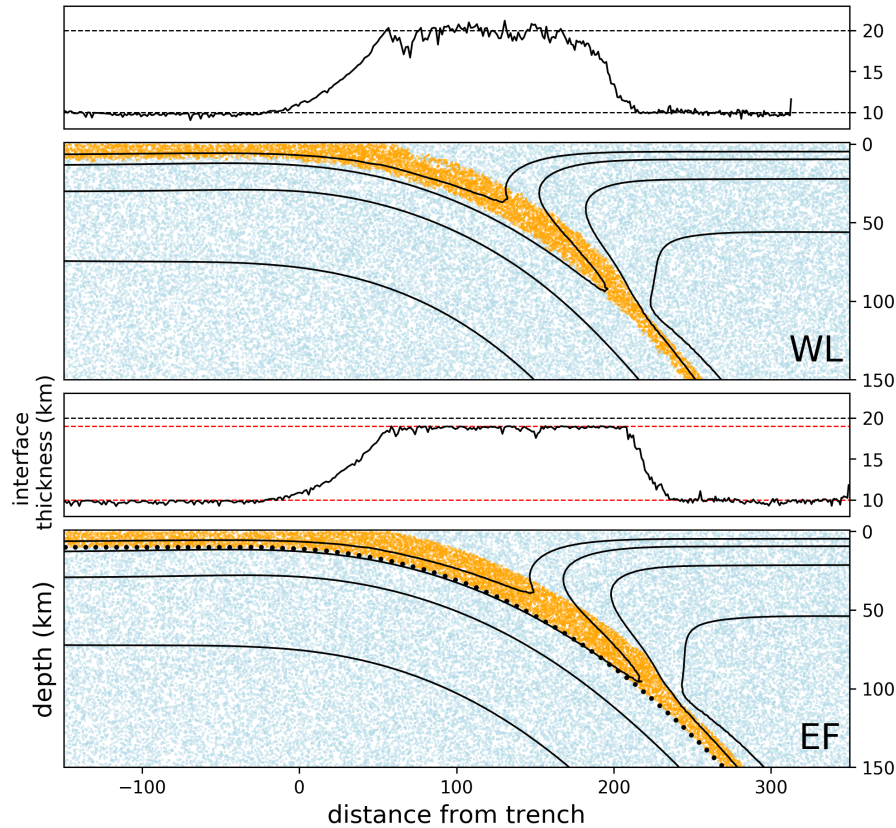


Figure 10. Distribution of subduction interface materials. Results from a standard WL model are shown in the top panel, EF model shown in bottom panel. Both models have a constant viscosity interface rheology. In the lower panels, orange points are the subduction interface material, blue points are the background material (mantle/lithosphere). Points in the material swarm and along the EF reference line have been down-sampled for clarity. Solid black lines over the material points are isotherms. Smaller panels show the measured interface thicknesses in each case; red horizontal lines show the thickness constraints W_{\min} , W_{\max} .

5.3 Stability and convergence

So far we have discussed results based on well-resolved models, with 160 elements across the 1000 km vertical domain. At this resolution, the vertically-refined mesh provides 3.2 elements within the subduction interface (at $W_{init} = 10$ km). Note that this increases to more than 6 elements in the decoupling zone, once the interface has thickened to ~ 20 km. We now look at the convergence of models under variable resolution, based on a standard WL approach as well as the EF implementation. Fig. 12 shows the slab temperature field, 10 Myr after the initiation of the model, for different models with varying resolution: 72, 96, 128, 160 elements in the vertical dimension. The ratio of the initial interface width (W_{init}) to the element width has values of 1.4, 1.9, 2.6, 3.2 for the respective mesh resolutions. The dashed slab outline in Fig. 12 shows the morphology for a simulation with 192 elements in the vertical dimension; this is used as a reference model in the following analysis. Note

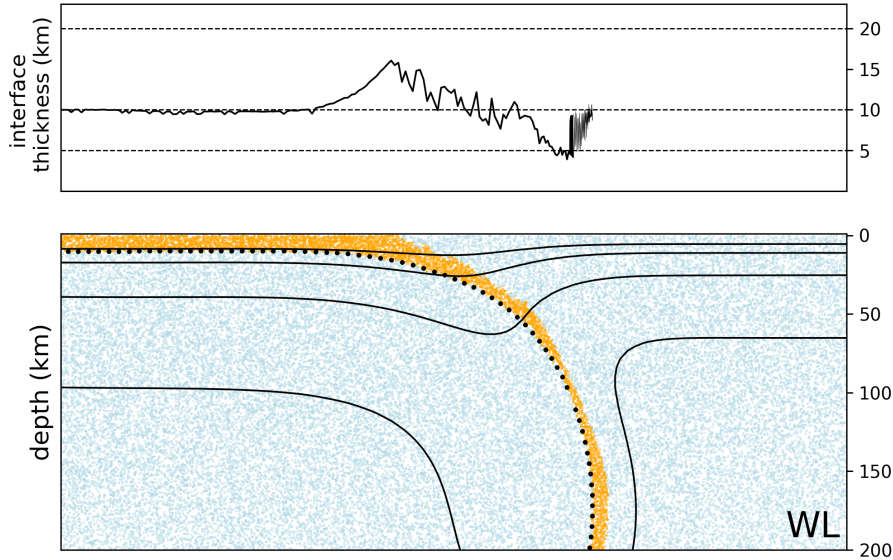


Figure 11. Interface thickness in under-resolved WL model. In the lower panel orange points show the subduction interface material, blue points are the background material (mantle/lithosphere). Upper panel shows interface thickness. Figure shows the model state 10 Myr after model initiation. This model is also shown in the upper-left panel of Fig. a.

that while we have varied the mesh resolution, all models have the same spatial particle density. Fig. 12a shows results using a standard WL implementation. At the lowest resolution (72 elements) the simulation stalls and undergoes runaway thermal decay. At 96 elements, the model is still strongly impacted by under-resolution of the subduction interface. Fig. 12b shows equivalent results using the EF implementation. Qualitatively, we see that EF models are more stable at lower resolution. For instance, the EF model at lowest resolution (72 elements) produces better results (closer to the reference model) than does the WL model with 96 elements.

Fig. 12 suggests that the EF models converge more closely with increasing resolution. We quantify this by tracking the relative error (L_2) of the temperature field in the lower resolution models with respect to the reference model (192 elements). The relative error with respect to the reference model (T_{ref}) is:

$$E = \left[\frac{\int_{\Omega} (T - T_{\text{ref}}) \cdot (T - T_{\text{ref}}) dV}{\int_{\Omega} T_{\text{ref}} \cdot T_{\text{ref}} dV} \right]^{1/2} \quad (1)$$

Fig. 13 shows relative error results for the same set of models shown in Fig. 12, confirming that the EF has better resolution convergence than the standard WL approach. For most of the models shown in Fig. 13 the relative error accumulates rapidly in the first 7-10 million years of the simulation, while the error rate flattens after this. This is similar to the time taken for the WL interface to reach its equilibrium thickness (e.g. Fig. 4). This suggests that models are particularly resolution-sensitive during the transient phase of the interface thickness adjustment. At low resolution (72, 96, 128 elements), errors in both WL



or EF models express this sensitivity. Interestingly, at 160 elements, the EF case exhibits nearly-constant error accumulation during the model evolution. This suggests that we have succeeded in reducing the sensitivity of the subduction interface implementation, relative to the overall error accumulation rate. The latter may be influenced by additional factors which we have not controlled for here, such as the timestep size in the advection-diffusion implementation which is controlled by the mesh resolution).

Fig. 11 shows the distribution of interface material in the lowest-resolution WL model (shown in the top left panel in Fig. 12a). In this case, under-resolution of the weak layer induces strong coupling between the slab and the upper plate at relatively shallow depths and begins to thin the WL, according to the principles outlined in Section 5. This induces further coupling and yet more thinning. This proves to be catastrophic feedback process, causing the simulation to stall and enter runaway thermal decay. The EF approach provides stability in this context, by inhibiting the feedback cycle. While this behavior is mainly relevant for models run at low resolution, the increased stability of the EF approach is a useful property, particularly from a model development perspective.

6 Discussion and Conclusions

The entrained weak layer (WL) is a common approach for implementing the subduction interface in long-term dynamic simulations. We have discussed aspects of WL implementation that can have an unintended impact on model evolution. The first involves the transient evolution of a uniform thickness interface to a variable thickness - uniform flux, configuration. If not properly accounted for, thinning of the deeper part of the WL could lead to numerical under-resolution, as previously suggested (Arcay, 2017). If the WL has a viscous rheology, the thinning will lead to higher stresses. This can induce a positive feedback when higher stresses increase the amount of partial coupling, inducing further thinning. Even for seemingly well-resolved models, the transient behavior of the subduction interface appears to be responsible for strong mesh sensitivity and poor resolution convergence. In general, models with plastic/frictional rheologies should be less sensitive to these transient adjustments, as the stress should not depend on the width of the interface.

Another tendency of the WL models is to develop persistent short wavelength thickness variations. These may represent interface instabilities, as are observed in Couette flows past a deformable boundary (Shankar and Kumar, 2004). These tend to dominate on the shallow part of the boundary with the upper plate. While flux-related thickness variation will be expected for any model implementation of WL, boundary instabilities (short wavelength) are likely to be more variable across different codes. They may depend on additional details of implementation, such as the rheology of the plates, material advection and interpolation schemes. Together, these issues are likely to hinder efforts to produce reproducible results between codes.

These unintended behaviors of the WL approach can be partly mitigated by controlling the thickness of the interface. We demonstrate a simple implementation of this concept, which utilises a line of reference points at the base of the WL. We call this approach an embedded fault (EF). The ability to constrain the thickness of the interface improves the resolution convergence of numerical models, as well as the stability at lower resolutions. The EF does add complexity to models, both in the sense of implementation as well as the introduction of new parameters to control the specific details (e.g. W_{\max}). There

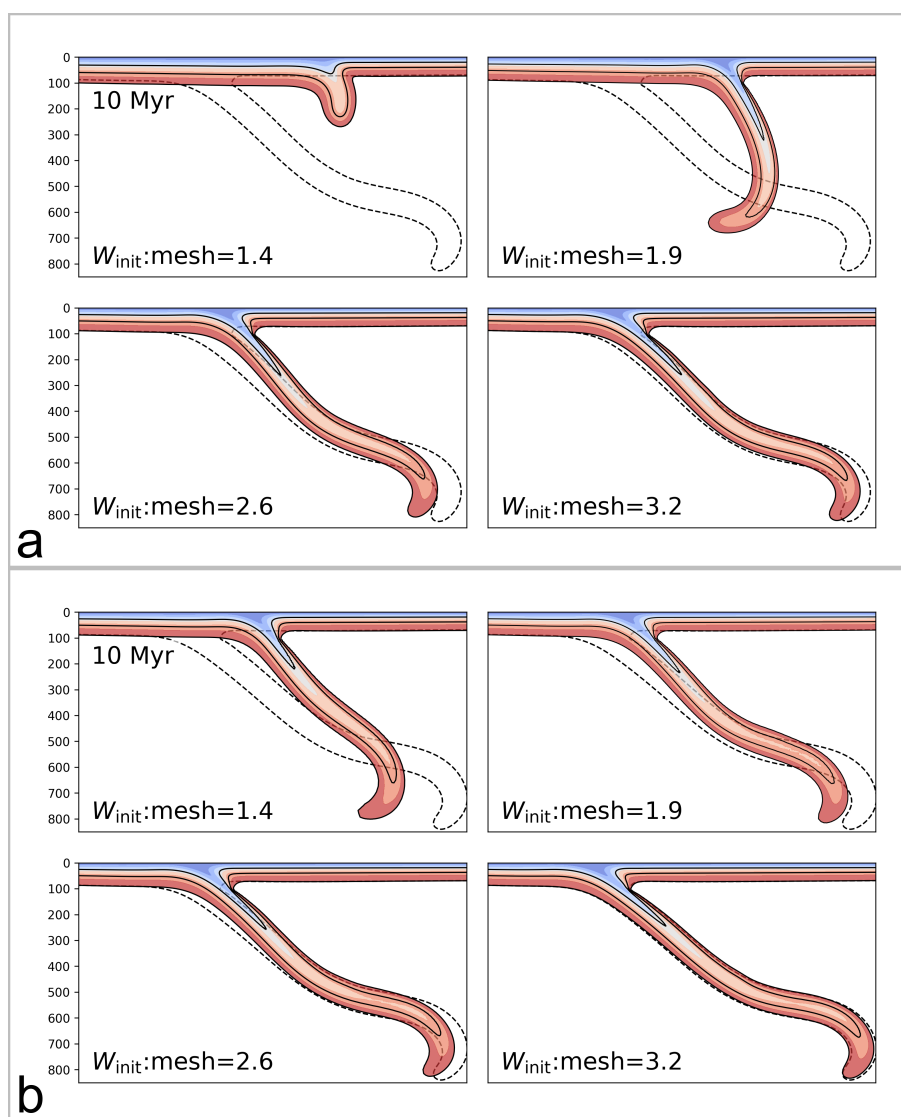


Figure 12. Model behaviour with variable resolution. Colormap shows slab temperature field at 10 Myr, masked above 1250 °C. Each figure shows a series of models run at different resolution. The total number of elements in the vertical coordinate was 96, 127, 160, 192. Corresponding subduction interface resolution is displayed in the figure, representing the initial fault thickness (W_{init}) divided by the local element size. a) models using standard WL implementation. b) models using the EF implementation.

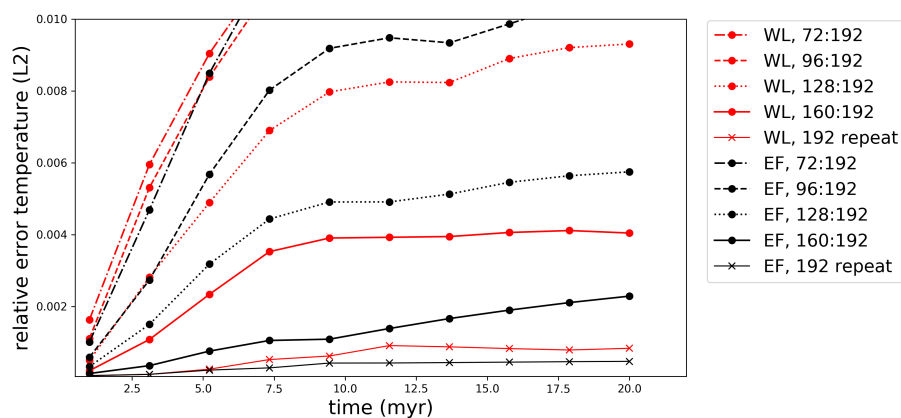


Figure 13. Convergence of models with varying resolution. Vertical axis shows the relative error (L_2) of the temperature field. We have truncated the vertical axis so as to focus on trends in the higher-resolution results. The error value is based on the error between the highest resolution model (192 elements in the vertical axis) and each of the models with lower resolution, as labelled in the figure. Experiments were repeated at the highest resolution to provide a baseline for model reproducibility (labelled ‘repeat’)

are obviously other implementation strategies that could be developed in order to achieve similar outcomes. These should be explored in future studies. Overall, this study provides a better understanding of the behaviour of subduction models utilising WL approaches. These insights offer a basis for achieving better outcomes in terms of model reproducibility and precision.



Appendix A: Governing equations, constitutive relationships and physical parameters

A1 Continuity, momentum and energy equations

On geological time scales the Earth's mantle behaves as a highly viscous, incompressible fluid, in which inertial forces can be neglected. The flow caused by internal buoyancy anomalies is described by the static force-balance (momentum conservation)

5 and continuity equations:

$$\sigma_{ij,j} + \rho g_i = 0 \quad (\text{A1})$$

$$u_{i,i} = 0 \quad (\text{A2})$$

where u_i is the i^{th} component of the velocity. Repeated indices denote summation, and $u_{,i}$ represents partial derivative with respect to the spatial coordinate x_i . The full stress tensor appearing in Eq.A1 can be decomposed into deviatoric and mean

10 (lithostatic) components:

$$\sigma_{ij} = \tau_{ij} + p\delta_{ij} \quad (\text{A3})$$

It is noted that sign of the pressure (p) is opposite to the mean stress tensor, consistent with the convention that fluid flows from high to low pressure. The deviatoric stress tensor (τ) and the strain rate tensor (D_{ij}) are related according to the constitutive relationship:

$$15 \quad \tau_{ij} = 2\eta D_{ij} = \eta(u_{i,j} + u_{j,i}) \quad (\text{A4})$$

Substituting Eqs.A4 & A3 into Eq.A1 gives the Stokes equation, which involves two unknown variables: pressure, and velocity. The Stokes and continuity equation are sufficient to solve for the two unknowns, together with appropriate boundary conditions. An approximate solution to these equations is derived using a Galerkin Finite Element method, implemented in the *Underworld 2* code.

20 The thermal evolution of the system expresses the balance between heat transport by fluid motion, thermal diffusion and internal heat generation by the 1st Law of Thermodynamics, assuming incompressibility:

$$\rho C_p \frac{DT}{Dt} = q_{i,i} + \rho Q \quad (\text{A5})$$



where T is the temperature and Q is the heat production rate (everywhere zero in this study). Diffusion rates are described by Fourier's Law, which satisfies the 2nd Law for positive conductivity (k):

$$q_i = -kT_{,i} \quad (\text{A6})$$

Inserting Eq.A6 into Eq.A5, and using the definition of the material derivative gives:

$$5 \quad \frac{\partial T}{\partial t} - u_i T_{,i} = (\kappa T_{,i})_{,i} + \frac{Q}{C_p} \quad (\text{A7})$$

where $\kappa = \frac{k}{\rho C_p}$ is the thermal diffusivity.

The thermal variations are coupled to the momentum equation through their effect on density. At pressures in planetary interiors, silicate minerals are weakly compressible and this is generally considered as a perturbation to an incompressible flow. The Boussinesq approximation accounts for the buoyancy forces while neglecting the associated volume change allowing us to assume incompressibility (Eq. A2). In the case of density variations due to temperature, the equation of state is:

$$\rho = \rho_0(1 - \alpha(T - T_p)) \quad (\text{A8})$$

where ρ_0 is the density at a reference temperature (here the mantle potential temperature T_p). α is the coefficient of thermal expansion. It is generally much smaller than one, making the Boussinesq approximation reasonable.

The equations and parameters that appear in the numerical models are based on equivalent dimensionless forms of the governing equations. We use the following characteristic scales (e.g Christensen, 1984):

$$\bar{x}_i = x_i \left[\frac{1}{d} \right], \quad \bar{u}_i = u_i \left[\frac{d}{\kappa} \right], \quad \bar{\eta} = \eta \left[\frac{1}{\eta_0} \right], \quad \bar{\tau} = \tau \left[\frac{d^2}{\kappa \eta_0} \right], \quad \bar{t} = t \left[\frac{\kappa}{d^2} \right], \quad \bar{T} = T \left[\frac{1}{\Delta T} \right], \quad (\text{A9})$$

where d is the mantle depth, t is time, η_0 is the reference viscosity and $\Delta T = (T_s - T_p)$, is the superadiabatic temperature difference across the fluid layer. Substituting dimensional terms for scaled dimensionless values (e.g $x \rightarrow \bar{x}d$), and rearranging allows us to write the Stokes equation as:

$$20 \quad 2\bar{\eta}\bar{D}_{ij,j} + \bar{p}_{,i} = Ra(1 - \bar{T})(-\delta_{iz}) \quad (\text{A10})$$

Overbars in Eq.A10 represent dimensionless quantities, and all dimensional parameters are contained in the dimensionless ratio Ra , the Rayleigh number which can be interpreted as a ratio of advection and diffusion timescales:

$$Ra = \frac{\rho_0 g \alpha \Delta T D^3}{\eta_0 \kappa} \quad (\text{A11})$$



The dimensionless viscosity, which has a functional dependence on the total pressure, the temperature and the second invariant of the stress tensor, are described below.

The dimensionless form of the heat conservation equation is:

$$\frac{\partial \bar{T}}{\partial t} - \bar{u}_i \bar{T}_{,i} = (\bar{T}_{,i})_{,i} + \bar{Q} \quad (\text{A12})$$

5 where the dimensionless internal heating is given by:

$$\bar{Q} = Q \left[\frac{d^2}{\kappa C_p \Delta T} \right] \quad (\text{A13})$$

A2 Rheology

Mantle silicates deform through a range of mechanisms. The most important high-temperature creep mechanisms are diffusion creep (low stress), which results in a linear relationship between stress and strain that is strongly dependent on grain size; and
 10 dislocation creep (high stress), which leads to a power law relationship between stress and strain that is independent of grain size. In addition to high-temperature creep, some form of stress limiting behaviour is expected to occur at low temperature, and high-stress. Glide-controlled dislocation creep (or Peierls creep), which includes a stress dependence of the activation energy, is likely to play a role, particularly in the cold part of subducted slabs Karato (2012). Nevertheless, it remains unclear whether
 15 Peierls creep allows sufficient weakening, as geophysical constraints on slabs would imply (e.g. Jain et al., 2017; Krien and Fleitout, 2008; Alisic et al., 2010). In geodynamic calculations, the effect of the Peierls mechanism is similar to that of plastic, temperature-independent plasticity models (Agrusta et al., 2017; Garel et al., 2014; Čížková and Bina, 2013).

To keep the models as simple as possible We include two deformation mechanism only: grainsize-independent diffusion creep and a plastic yielding based on a truncated Drucker-Prager plasticity model. The plastic strain rates are capable of representing brittle failure at low pressure (near the surface) and low-temperature plasticity at high pressure (deep within the
 20 slab). The value of the yield stress limit is chosen on the basis of previous studies, and is consistent with several lines of evidence suggesting that slabs to not support more than a few hundred MPa (Richards et al., 2001; Tackley, 2000; Watts and Zhong, 2000; Krien and Fleitout, 2008; Alisic et al., 2010). The viscosity associated with each deformation mechanism is combined using a harmonic average, denoted by η_c . The entire computational domain, except for the subduction interface, is governed by the same composite rheology: there is no compositional distinction between the mantle and plates.

25 Ductile flow laws for silicates often have an Arrhenius temperature and pressure dependence, controlled by the activation energy E , and activation volume V (Hirth and Kohlstedt, 2004). Additional dependencies, such as grain size and melt fraction, are neglected in this study, resulting in the following diffusion viscosity:

$$\eta_d = A \exp \left(\frac{E + p_l V}{RT_a} \right) \quad (\text{A14})$$



where p_l indicates the lithostatic component of the pressure, and A is a constant. A linearised adiabatic term is added to the dimensionless temperature field, whenever it appears in an Arrhenius law:

$$T_a = T + z \times T_{,z}$$

$$T_{,z} = \frac{-\alpha g T_p}{C_p}$$

The dimensionless form of the creep law applied in the models uses the following scalings:

$$5 \quad \bar{E} = E \left[\frac{1}{R\Delta T} \right], \quad \bar{W} = V \left[\frac{\rho_0 g d}{R\Delta T} \right], \quad \bar{A} = A \left[\frac{1}{\eta_0} \right] \quad (\text{A15})$$

Note that $V \rightarrow \bar{W}$ includes a change from pressure dependence (dimensional) to depth dependence (dimensionless): The dimensionless diffusion creep viscosity can be written:

$$\bar{\eta}_d = \bar{A} \exp \left(\frac{\bar{E} + \bar{z}\bar{W}}{\bar{T}_s + \bar{T}_a} \right) \quad (\text{A16})$$

where \bar{z} is the dimensionless depth and \bar{T}_s is the dimensionless surface temperature. The dimensionless linearised adiabatic component is incorporated as follows:

$$\bar{T}_a = \bar{T} + \bar{z} \times \bar{T}_{,\bar{z}}$$

$$\bar{T}_{,\bar{z}} = T_{,z} \left[\frac{d}{\Delta T} \right]$$

The parameters chosen for the diffusion creep law are consistent with those derived from experimental data on dry olivine (Karato and Wu, 1993), providing an average upper mantle viscosity close to 1×10^{20} Pa.s. The relatively high value of the activation volume produces relatively low viscosity asthenosphere $\sim 0.3 \times 10^{20}$, relative to the transition zone $\sim 5 \times 10^{20}$.
 15 Additionally, a viscosity increase ($\times \eta_{660}$) is applied at the 660 km discontinuity, consistent with inferences based on the geoid (Hager and O'Connell, 1981). For ($\times \eta_{660} = 10$), the lower mantle just beneath the 660 km is 50 times more viscous than the mean viscosity of the upper mantle. The parameters chosen produce radial viscosity profiles that are slightly higher than the 'Haskell constraint' ($\eta_{\text{mean}} = 1 \times 10^{21}$) over the upper 1400 km of the mantle (e.g. Becker, 2017).

A range of psuedo-brittle and plastic deformation mechanisms can be approximated in the fluid constitutive model by
 20 allowing non-linearity in the viscosity ($\eta = \eta(T, p, J_I, \dots)$). The rheological model itself should be defined independently of the coordinate system, so it is necessary to define the constitutive model in terms of stress invariants (J_I). The standard viscoplastic approach (Spiegelman et al., 2016) defines an effective plastic viscosity η_p such that the deviatoric stress tensor is bounded by a yield stress τ_y :

$$\tau_y = 2\eta_p D_{ij} \quad (\text{A17})$$



Assuming that η_p is isotropic and scalar (i.e. eigenvectors of the strain-rate tensor and deviatoric stress are identical), one can use the magnitude of both sides to define the scalar effective plastic viscosity as:

$$\eta_p = \frac{\tau_{y(II)}}{2\epsilon_{II}} \quad (\text{A18})$$

where the subscript II, denotes the square root of the tensor second invariant.

- 5 The yield stress function in the computational models is a truncated Drucker-Prager criterion:

$$\tau_y = \min(\tau_{\max}, \mu p + C) \quad (\text{A19})$$

where μ is the friction coefficient, and C is the cohesion. The Drucker-Prager yield surface is defined by the full pressure p . Because the pressure that appears in the dimensionless Stokes equation (Eq. A10) is a dynamic pressure (\bar{p}), due to density variations only, the lithostatic pressure (a function of vertical coordinate) needs to be accounted for. The dimensionless form

- 10 of the yield stress is given by

$$\bar{\tau}_y = \min(\bar{\tau}_{\max}, \bar{\mu}(\bar{p} + \bar{p}_l \bar{z}) + \bar{C}) \quad (\text{A20})$$

where:

$$\begin{aligned} \bar{\mu} &= \mu, \\ \bar{C} &= C \left[\frac{d^2}{\kappa \eta_0} \right], \\ \bar{\tau}_{\max} &= \tau_{\max} \left[\frac{d^2}{\kappa \eta_0} \right], \\ \bar{P}_l &= \bar{z} \left[\frac{\rho_0 g d^3}{\kappa \eta_0} \right], \end{aligned} \quad (\text{A21})$$

The effective plastic viscosity (dimensionless) is given by:

15
$$\bar{\eta}_p = \frac{\bar{\tau}_{y(II)}}{2\dot{\epsilon}_{II}} \quad (\text{A22})$$

The final (composite) viscosity is the harmonic average of the viscosity associated with creep and plastic yielding:

$$\bar{\eta}_c = \frac{\bar{\eta}_d \bar{\eta}_p}{\bar{\eta}_d + \bar{\eta}_p} \quad (\text{A23})$$



A3 Model parameters and scaling values

This section provides a record of model parameters and reference values that are used in the models. The dimensional parameters quoted here are non-dimensionalised using the scaling system described in Appendix A and reference values provided in Table A1. This scaling system is identical for all models used within the thesis.

| Reference value | Value | Symbol | Units |
|---------------------|--------------------|------------|-----------------------------------|
| length | 2900 | d | km |
| viscosity | 1×10^{20} | η_0 | Pas |
| density | 3300 | ρ_0 | kg m^{-3} |
| thermal diffusivity | 1×10^{-6} | κ | $\text{m}^2 \text{s}^{-1}$ |
| gravity | 9.8 | g | m s^{-2} |
| temperature | 1400 | ΔT | K |
| gas constant | 8.314 | R | $\text{J mol}^{-1} \text{K}^{-1}$ |
| Rayleigh Number | 3.31×10^8 | Ra | - |

Table A1. Reference values used to non-dimensionalise the Stokes and Energy equations, as described in Appendix A



| Parameter name | Value | Symbol | Units |
|----------------------------------|-----------------------|---------------------|------------------------------|
| domain depth | 100 | - | km |
| domain width | 5000 | - | km |
| potential temp | 1673 | T_p | K |
| surface temp | 273 | T_s | K |
| viscosity min. | 1×10^{18} | - | Pa.s |
| viscosity max. | 1×10^{24} | - | Pa.s |
| diffusion creep volume UM** | 5.27×10^{-6} | V | $\text{m}^3 \text{mol}^{-1}$ |
| diffusion creep energy UM | 316 | E | kJ mol^{-1} |
| diffusion creep constant UM | 1.87×10^9 | A | $\text{Pa}^n \text{s}^1$ |
| diffusion creep volume LM*** | 1.58×10^{-6} | V | $\text{m}^3 \text{mol}^{-1}$ |
| diffusion creep energy LM | 210 | E | kJ mol^{-1} |
| diffusion creep constant LM | 1.77×10^{14} | A | $\text{Pa}^n \text{s}^1$ |
| DP* friction coefficient | 0.1 | μ | - |
| DP cohesion | 20 | C | MPa |
| yield stress max. | 200 | τ_{max} | MPa |
| sub. interface thickness | 10 | W_{init} | km |
| sub. interface max. thickness | 19 | W_{max} | km |
| sub. interface min. thickness | 10 | W_{min} | km |
| sub. interface viscosity | 5×10^{19} | - | Pa.s |
| sub. interface depth taper start | 100 | - | km |
| sub. interface depth taper width | 30 | - | km |
| slab age at trench | 50 | - | Myr |
| slab radius of curv. | 200 | - | km |
| initial slab depth | 150 | - | km |
| upper plate age at trench | 10 | - | Myr |
| lower mantle viscosity increase | 15 | - | - |
| adiabatic temp. gradient | 3.7×10^{-4} | - | - |
| internal heating | 0.0 | Q | W.m^{-3} |

Table A2. Dimensional model parameters: * Drucker-Prager, ** Upper Mantle, *** Lower mantle. Typical model element resolution was 800×160 .



Competing interests. TEXT

The authors declare that no competing interests are present.

Acknowledgements. This research was partially funded by the Australian Government through the Australian Research Council Discovery grant DP150102887. Development of the Underworld2 code used in the simulations supported by AuScope. Dan's postgraduate research at the University of Melbourne was supported by a Baragwanath Geology Research Scholarship. The study benefited from the authors' attendance of the CIDER Summer programs in 2016 & 2017 (funded by NSF grant EAR-1135452). This work was supported by resources provided by The Pawsey Supercomputing Centre with funding from the Australian Government and the Government of Western Australia. This research was supported by use of the Nectar Research Cloud, a collaborative Australian research platform supported by the National Collaborative Research Infrastructure Strategy (NCRIS).



References

- Aagaard, B., Williams, C., and Knepley, M.: PyLith: A finite-element code for modeling quasi-static and dynamic crustal deformation, *Eos Trans. AGU*, 89, 2008.
- Abers, G. A.: Seismic low-velocity layer at the top of subducting slabs: observations, predictions, and systematics, *Physics of the Earth and Planetary Interiors*, 149, 7–29, 2005.
- 5 Agrusta, R., Goes, S., and van Hunen, J.: Subducting-slab transition-zone interaction: Stagnation, penetration and mode switches, *Earth and Planetary Science Letters*, 464, 10–23, 2017.
- Alisic, L., Gurnis, M., Stadler, G., Burstedde, C., Wilcox, L. C., and Ghattas, O.: Slab stress and strain rate as constraints on global mantle flow, *Geophysical Research Letters*, 37, <https://doi.org/10.1029/2010gl045312>, <http://dx.doi.org/10.1029/2010gl045312>, 2010.
- 10 Androvičová, A., Čížková, H., and van den Berg, A.: The effects of rheological decoupling on slab deformation in the Earth's upper mantle, *Studia Geophysica et Geodaetica*, 57, 460–481, 2013.
- Arcay, D.: Dynamics of interplate domain in subduction zones: influence of rheological parameters and subducting plate age, *Solid Earth*, 3, 467, 2012.
- Arcay, D.: Modelling the interplate domain in thermo-mechanical simulations of subduction: Critical effects of resolution and rheology, and consequences on wet mantle melting, *Physics of the Earth and Planetary Interiors*, 269, 112–132, 2017.
- 15 Arnold, D. N. and Logg, A.: Periodic table of the finite elements, *SIAM News*, 47, 212, 2014.
- Arredondo, K. M. and Billen, M. I.: Coupled Effects of Phase Transitions and Rheology in 2D Dynamical Models of Subduction, *Journal of Geophysical Research: Solid Earth*, 2017.
- Audet, P. and Schwartz, S. Y.: Hydrologic control of forearc strength and seismicity in the Costa Rican subduction zone, *Nature Geoscience*, 20 6, 852, 2013.
- Audet, P., Bostock, M. G., Christensen, N. I., and Peacock, S. M.: Seismic evidence for overpressured subducted oceanic crust and megathrust fault sealing, *Nature*, 457, 76–78, 2009.
- Babeyko, A. and Sobolev, S.: High-resolution numerical modeling of stress distribution in visco-elasto-plastic subducting slabs, *Lithos*, 103, 205–216, 2008.
- 25 Bachmann, R., Oncken, O., Glodny, J., Seifert, W., Georgieva, V., and Sudo, M.: Exposed plate interface in the European Alps reveals fabric styles and gradients related to an ancient seismogenic coupling zone, *Journal of Geophysical Research: Solid Earth*, 114, 2009.
- Bayet, L., John, T., Agard, P., Gao, J., and Li, J.-L.: Massive sediment accretion at ~ 80 km depth along the subduction interface: Evidence from the southern Chinese Tianshan, *Geology*, 2018.
- Bebout, G. E. and Penniston-Dorland, S. C.: Fluid and mass transfer at subduction interfaces, The field metamorphic record, *Lithos*, 240, 30 228–258, 2016.
- Becker, T. W.: Superweak asthenosphere in light of upper mantle seismic anisotropy, *Geochemistry, Geophysics, Geosystems*, 18, 1986–2003, 2017.
- Behr, W. M. and Becker, T. W.: Sediment control on subduction plate speeds, *Earth and Planetary Science Letters*, 502, 166–173, <https://doi.org/10.1016/j.epsl.2018.08.057>, 2018.
- 35 Bercovici, D.: The generation of plate tectonics from mantle convection, *Earth and Planetary Science Letters*, 205, 107–121, 2003.
- Bercovici, D. and Ricard, Y.: Plate tectonics damage and inheritance, *Nature*, 508, 513–516, <https://doi.org/10.1038/nature13072>, <http://dx.doi.org/10.1038/nature13072>, 2014.



- Billen, M. I. and Hirth, G.: Rheologic controls on slab dynamics, *Geochemistry Geophysics, Geosystems*, 8, <https://doi.org/10.1029/2007gc001597>, <http://dx.doi.org/10.1029/2007gc001597>, 2007.
- Billen, M. I., Gurnis, M., and Simons, M.: Multiscale dynamics of the Tonga-Kermadec subduction zone, *Geophysical Journal International*, 153, 359–388, 2003.
- 5 Brooks, A. N. and Hughes, T. J.: Streamline upwind/Petrov-Galerkin formulations for convection dominated flows with particular emphasis on the incompressible Navier-Stokes equations, *Computer methods in applied mechanics and engineering*, 32, 199–259, 1982.
- Buiter, S. and Ellis, S.: A discussion of numerical subduction initiation, in: *EGU General Assembly Conference Abstracts*, vol. 18, p. 4791, 2016.
- Capitanio, F., Stegman, D., Moresi, L., and Sharples, W.: Upper plate controls on deep subduction, trench migrations and deformations at
10 convergent margins, *Tectonophysics*, 483, 80–92, 2010.
- Chertova, M., Geenen, T., Van Den Berg, A., and Spakman, W.: Using open sidewalls for modelling self-consistent lithosphere subduction dynamics, *Solid Earth*, 3, 313, 2012.
- Christensen, U.: Convection with pressure- and temperature-dependent non-Newtonian rheology, *Geophysical Journal International*, 77, 343–384, 1984.
- 15 Christensen, U. R.: The influence of trench migration on slab penetration into the lower mantle, *Earth and Planetary Science Letters*, 140, 27–39, 1996.
- Čížková, H. and Bina, C. R.: Effects of mantle and subduction-interface rheologies on slab stagnation and trench rollback, *Earth and Planetary Science Letters*, 379, 95–103, 2013.
- Čížková, H., van Hunen, J., van den Berg, A. P., and Vlaar, N. J.: The influence of rheological weakening and yield stress on the interaction
20 of slabs with the 670 km discontinuity, *Earth and Planetary Science Letters*, 199, 447–457, 2002.
- Cloos, M. and Shreve, R. L.: Subduction-channel model of prism accretion, melange formation, sediment subduction, and subduction erosion at convergent plate margins: 1. Background and description, *Pure and Applied Geophysics*, 128, 455–500, 1988.
- Duarte, J. C., Schellart, W. P., and Cruden, A. R.: How weak is the subduction zone interface?, *Geophysical Research Letters*, 42, 2664–2673, 2015.
- 25 Duretz, T., Schmalholz, S. M., and Gerya, T. V.: Dynamics of slab detachment, *Geochemistry Geophysics, Geosystems*, 13, <https://doi.org/10.1029/2011gc004024>, <http://dx.doi.org/10.1029/2011gc004024>, 2012.
- Gao, X. and Wang, K.: Strength of stick-slip and creeping subduction megathrusts from heat flow observations, *Science*, 345, 1038–1041, 2014.
- Garel, F., Goes, S., Davies, D. R., Davies, J. H., Kramer, S. C., and Wilson, C. R.: Interaction of subducted slabs with the mantle transition-
30 zone: A regime diagram from 2-D thermo-mechanical models with a mobile trench and an overriding plate, *Geochemistry Geophysics, Geosystems*, 15, 1739–1765, <https://doi.org/10.1002/2014gc005257>, <http://dx.doi.org/10.1002/2014gc005257>, 2014.
- Gerardi, G. and Ribe, N. M.: Boundary-element modeling of two-plate interaction at subduction zones: scaling laws and application to the Aleutian subduction zone, *Journal of Geophysical Research: Solid Earth*, 2018.
- Gerya, T. V., Stöckhert, B., and Perchuk, A. L.: Exhumation of high-pressure metamorphic rocks in a subduction channel: A numerical
35 simulation, *Tectonics*, 21, 2002.
- Gerya, T. V., Connolly, J. A., and Yuen, D. A.: Why is terrestrial subduction one-sided?, *Geology*, 36, 43–46, 2008.



- Glerum, A., Thieulot, C., Fraters, M., Blom, C., and Spakman, W.: Implementing nonlinear viscoplasticity in ASPECT: benchmarking and applications to 3D subduction modeling, *Solid Earth Discussions*, 2017, 1–47, <https://doi.org/10.5194/se-2017-9>, <https://www.solid-earth-discuss.net/se-2017-9/>, 2017.
- Gurnis, M. and Hager, B. H.: Controls of the structure of subducted slabs, *Nature*, 335, 317–321, 1988.
- 5 Hager, B. H. and O'Connell, R. J.: A simple global model of plate dynamics and mantle convection, *Journal of Geophysical Research*, 86, 4843, <https://doi.org/10.1029/jb086ib06p04843>, <http://dx.doi.org/10.1029/jb086ib06p04843>, 1981.
- Hardebeck, J. L.: Stress orientations in subduction zones and the strength of subduction megathrust faults, *Science*, 349, 1213–1216, 2015.
- Hardebeck, J. L. and Loveless, J. P.: Creeping subduction zones are weaker than locked subduction zones, *Nature Geoscience*, 11, 60, 2018.
- Hilaliret, N. and Reynard, B.: Stability and dynamics of serpentinite layer in subduction zone, *Tectonophysics*, 465, 24–29, 2009.
- 10 Hirauchi, K.-i. and Katayama, I.: Rheological contrast between serpentine species and implications for slab–mantle wedge decoupling, *Tectonophysics*, 608, 545–551, 2013.
- Hirth, G. and Kohlstedt, D.: Rheology of the upper mantle and the mantle wedge: A view from the experimentalists, *Inside the subduction Factory*, 138, 83–105, 2004.
- Holt, A. F., Buffett, B. A., and Becker, T. W.: Overriding plate thickness control on subducting plate curvature, *Geophysical Research Letters*, 15 42, 3802–3810, 2015.
- Huene, R. and Scholl, D. W.: Observations at convergent margins concerning sediment subduction, subduction erosion, and the growth of continental crust, *Reviews of Geophysics*, 29, 279–316, 1991.
- Jain, C., Korenaga, J., and Karato, S.-i.: On the yield strength of oceanic lithosphere, *Geophysical Research Letters*, 44, 9716–9722, 2017.
- Karato, S.-i.: Deformation of earth materials: an introduction to the rheology of solid Earth, 2012.
- 20 Karato, S.-i. and Wu, P.: Rheology of the upper mantle: A synthesis, *Science*, 260, 771–778, 1993.
- Kimura, G., Yamaguchi, A., Hojo, M., Kitamura, Y., Kameda, J., Ujiie, K., Hamada, Y., Hamahashi, M., and Hina, S.: Tectonic mélange as fault rock of subduction plate boundary, *Tectonophysics*, 568, 25–38, 2012.
- Kincaid, C. and Sacks, I. S.: Thermal and dynamical evolution of the upper mantle in subduction zones, *Journal of Geophysical Research: Solid Earth*, 102, 12 295–12 315, 1997.
- 25 Krien, Y. and Fleitout, L.: Gravity above subduction zones and forces controlling plate motions, *Journal of Geophysical Research: Solid Earth*, 113, 2008.
- Lallemand, S.: High rates of arc consumption by subduction processes: Some consequences, *Geology*, 23, 551–554, 1995.
- Lamb, S.: Shear stresses on megathrusts: Implications for mountain building behind subduction zones, *Journal of Geophysical Research: Solid Earth*, 111, 2006.
- 30 Lenardic, A. and Kaula, W.: Self-lubricated mantle convection: Two-dimensional models, *Geophysical research letters*, 21, 1707–1710, 1994.
- Li, B. and Ghosh, A.: Near-continuous tremor and low frequency earthquake (LFE) activities in the Alaska-Aleutian subduction zone revealed by a mini seismic array, *Geophysical Research Letters*, 2017.
- Magni, V. v., Van Hunen, J., Funicello, F., and Faccenna, C.: Numerical models of slab migration in continental collision zones, *Solid Earth*, 3, 293, 2012.
- 35 Manea, V. and Gurnis, M.: Subduction zone evolution and low viscosity wedges and channels, *Earth and Planetary Science Letters*, 264, 22–45, 2007.



- Moresi, L. and Solomatov, V.: Mantle convection with a brittle lithosphere: thoughts on the global tectonic styles of the Earth and Venus, *Geophys. J. Int.*, 133, 669–682, <https://doi.org/10.1046/j.1365-246x.1998.00521.x>, <http://dx.doi.org/10.1046/j.1365-246x.1998.00521.x>, 1998.
- Peacock, S. M.: Thermal and petrologic structure of subduction zones, *Subduction top to bottom*, pp. 119–133, 1996.
- 5 Plank, T. and Langmuir, C. H.: Tracing trace elements from sediment input to volcanic output at subduction zones, *Nature*, 362, 739–743, 1993.
- Proctor, B. and Hirth, G.: Ductile to brittle transition in thermally stable antigorite gouge at mantle pressures, *Journal of Geophysical Research: Solid Earth*, 121, 1652–1663, 2016.
- Reynard, B.: Serpentine in active subduction zones, *Lithos*, 178, 171–185, 2013.
- 10 Richards, M. A., Yang, W.-S., Baumgardner, J. R., and Bunge, H.-P.: Role of a low-viscosity zone in stabilizing plate tectonics: Implications for comparative terrestrial planetology, *Geochemistry, Geophysics, Geosystems*, 2, 2001.
- Schellart, W. and Rawlinson, N.: Global correlations between maximum magnitudes of subduction zone interface thrust earthquakes and physical parameters of subduction zones, *Physics of the Earth and Planetary Interiors*, 225, 41–67, 2013.
- Schmidt, M. W. and Poli, S.: Experimentally based water budgets for dehydrating slabs and consequences for arc magma generation, *Earth and Planetary Science Letters*, 163, 361–379, 1998.
- 15 Shankar, V. and Kumar, L.: Stability of two-layer Newtonian plane Couette flow past a deformable solid layer, *Physics of Fluids*, 16, 4426–4442, 2004.
- Shreve, R. L. and Cloos, M.: Dynamics of sediment subduction, melange formation, and prism accretion, *Journal of Geophysical Research: Solid Earth*, 91, 10 229–10 245, 1986.
- 20 Spiegelman, M., May, D. A., and Wilson, C. R.: On the solvability of incompressible Stokes with viscoplastic rheologies in geodynamics, *Geochemistry, Geophysics, Geosystems*, 17, 2213–2238, 2016.
- Tackley, P. J.: Self-consistent generation of tectonic plates in time-dependent, three-dimensional mantle convection simulations, *Geochemistry, Geophysics, Geosystems*, 1, 2000.
- Tagawa, M., Nakakuki, T., Kameyama, M., and Tajima, F.: The role of history-dependent rheology in plate boundary lubrication for generating one-sided subduction, *Pure and Applied Geophysics*, 164, 879–907, 2007.
- 25 Trompert, R. and Hansen, U.: Mantle convection simulations with rheologies that generate plate-like behaviour, *Nature*, 395, 686, 1998.
- Ulmer, P., Trommsdorff, V., et al.: Serpentine stability to mantle depths and subduction-related magmatism, *Science*, pp. 858–858, 1995.
- van Keken, P. E., Currie, C., King, S. D., Behn, M. D., Cagnioncle, A., He, J., Katz, R. F., Lin, S.-C., Parmentier, E. M., Spiegelman, M., et al.: A community benchmark for subduction zone modeling, *Physics of the Earth and Planetary Interiors*, 171, 187–197, 2008.
- 30 Vannucchi, P., Remitti, F., and Bettelli, G.: Geological record of fluid flow and seismogenesis along an erosive subducting plate boundary, *Nature*, 451, 699, 2008.
- Vannucchi, P., Sage, F., Phipps Morgan, J., Remitti, F., and Collot, J.-Y.: Toward a dynamic concept of the subduction channel at erosive convergent margins with implications for interplate material transfer, *Geochemistry, Geophysics, Geosystems*, 13, 2012.
- Vrolijk, P.: On the mechanical role of smectite in subduction zones, *Geology*, 18, 703–707, 1990.
- 35 Wada, I. and Wang, K.: Common depth of slab-mantle decoupling: Reconciling diversity and uniformity of subduction zones, *Geochemistry, Geophysics, Geosystems*, 10, 2009.
- Wang, K.: Finding fault in fault zones, *Science*, 329, 152–153, 2010.



Watts, A. and Zhong, S.: Observations of flexure and the rheology of oceanic lithosphere, *Geophysical Journal International*, 142, 855–875, 2000.

Zhong, S. and Gurnis, M.: Viscous flow model of a subduction zone with a faulted lithosphere: Long and short wavelength topography gravity and geoid, *Geophysical Research Letters*, 19, 1891–1894, <https://doi.org/10.1029/92gl02142>, <http://dx.doi.org/10.1029/92gl02142>, 1992.

5 Zhong, S. and Gurnis, M.: Mantle Convection with Plates and Mobile Faulted Plate Margins, *Science*, 267, 838–843, <https://doi.org/10.1126/science.267.5199.838>, <http://dx.doi.org/10.1126/science.267.5199.838>, 1995.